

Article

Modeling and Simulation of Planing-Hull Watercraft Outfitted with an Electric Motor Drive and a Surface-Piercing Propeller

Nikolaos I. Xiros ^{1,*}, Vasileios Tzelepis ¹ and Eleftherios K. Loghis ²

¹ School of Naval Architecture and Marine Engineering, University of New Orleans, New Orleans, LA 70148, USA; vtzelepi@uno.edu

² School of Electrical and Computer Engineering, National Technical University of Athens, Zografou 15780, Greece; loghis_el@yahoo.gr

* Correspondence: nxiros@uno.edu; Tel.: +1-504-280-3130

Received: 26 December 2018; Accepted: 8 February 2019; Published: 18 February 2019



Abstract: A simulation model for a prismatic hard-chine planing hull watercraft (V-shaped keel with constant deadrise) with propulsion based on a 3-phase induction motor connected directly to surface-piercing propeller (SPP) and outfitted with a motor rotational speed controller was investigated, tested, and tuned. The modularity of the model developed enables straightforward substitution of diverse and more refined modules, or even attachment of additional ones to obtain greater level of detail or simulate more complicated processes. Industry trends do suggest an increasing interest in all-electric ship development as well as the use of surface-piercing propellers for small or medium-size craft. All-electric drive plants offer distinct advantages due to their flexibility in arrangements, ability to eliminate reduction gears in many cases, low maintenance requirements and wide range of available sizes as well superb load acceptance and dynamic matching to changing operational conditions. Employing electric drives onboard small craft with planing-hulls that achieve significantly higher velocities where arrangements and maneuverability are of critical design issues is a theme that has received increased attention by designers in recent years. Refined speed regulation and tracking compounded by the feature to produce fairly constant torque across a broad speed (rpm) range enables using of unconventional thrusters such as surface-piercing propellers to small craft. By investigating towing tank test data series for a surface-piercing propeller, development of a numerical simulation tool for unconventional thrusters was demonstrated. The surface-piercing propeller simulation model, as an artificial neural network (ANN), was coupled with a 3-phase induction motor as prime mover as well as dynamic propulsion shaft model and proportional-integral-differential (PID) controller. The various sub-models were finally integrated with a sub-model implementing Savitsky's propulsion resistance method and calculation of equilibrium trim for planing hull modeling. Simulations were conducted using full-scale real-world conditions for a high-speed small craft developed for leisure and sporting activities, rapid close-range transit, reconnaissance and surveying etc. The planing-hull watercraft considered is amenable to minor hull modifications in order to house a 50 kW electric motor and a four bladed surface-piercing propeller. Simulations performed allowed a full assessment of model functionality as well as level of detail.

Keywords: surface-piercing propeller; artificial neural net; induction motor; planing hull; shaft vibration model

1. Introduction

The main design consideration for any watercraft propulsion power plant is to enable the craft at required advance speed, and also generate thrust for maneuvering, stopping and backing [1]. In effect, a propulsion system typically includes the following four subsystems: the prime mover, the mechanical transmission system penetrating the hull, the thruster, and means for system control. The prime mover needs to generate sufficient power within the desired rpm range to overcome any load applied by the thruster. The mechanical transmission system, conventionally a propeller shaft, transmits power from the prime mover to the thruster and then thrust from the thruster to the craft's thrust bearing. The thruster develops sufficient thrust for the watercraft to advance forward as well as support maneuvering. Of equally great importance, an appropriate control system capable of conveying and translating the human operator's commands to the propulsion power-plant as a system is required. In effect these parts need to work in concert in order to generate and transmit torque and rotational power, then convert those to thrust and effectively kinetic energy of the vessel as well as maintain sufficient control over the energy flow and effective watercraft motion.

Configuration of a watercraft propulsion plant starts by selecting the vessel's service (nominal) forward speed (velocity). Such speed requirement is employed along with the hull form and watercraft mission to decide the resistance of the craft. Determining watercraft resistance is conducted using standard data series such as the Taylor series or Series 60; at later stages, numerical modeling such as computational fluid dynamics (CFD), or scale resistance tests in a towing tank are also routinely employed. The methodological steps are well established and fairly common in practice within the naval architecture discipline. Once the resistance of the vessel has been determined and safety margins such as weather and propeller-hull fouling have been accounted for, one or more thrusters are selected accommodating the required forward advance speed and resistance coefficients. Given a thruster choice, torque demand as function of its rotational speed (rpm) is required to then proceed to propeller shaft configuration and prime mover matching. Nowadays, the state of the art uses standardized yet empirical equations established by institutions such as the American Bureau of Shipping (ABS). In effect, torque demand curves are available for tested and broadly used thrusters. Also, torque delivery curves for a wide variety of commonly employed prime movers, as well as refined finite element models.

It is the objective of this investigation to formulate such a methodology for a new type of propulsion plants that are targeted for outfitting high-speed, planing-hull watercraft and include electric motors as prime movers and surface-piercing propellers (SPP) [2] as thrusters. Furthermore the objective is to model and simulate the watercraft propulsion power-plant in an integrated, modular fashion enabling simple swapping between various subsystems with others in order to enable comparative assessment. Of the utmost significance to the modeling analysis was the drive to include the control system outfit as an integral element of the configuration of the propulsion power plant in order to account for its complexities early in the design.

The research objectives were: (a) build a numerical model of a watercraft propulsion power-plant enabling for modular subsystem models; (b) establish a methodology to convert measured performance data for unconventional thrusters into a closed form mathematical expression complying with basic continuity and differentiability requirements at least within the speed and power range of interest for the thruster in question, so that a thruster model is developed; then develop a similar methodology to hydrodynamic resistance data obtained experimentally to non-standard hull types e.g., planing; (c) build and incorporate an electric motor model, a propeller shaft model, a surface-piercing propeller model and a planing-hull hydrodynamic model to establish through simulations the flexibility and usability of the full system model.

An all-electric shipboard propulsion powertrain typically includes electric motor(s), transmission shaft-line(s) and propeller(s) or thruster(s); a power-generation plant or electrical energy storage is needed to power the system [3]. When properly configured and designed, electric drives do away with the requirement for reduction and reversing gears and lead to a propulsion power-plant with

rather broad speed and operational range. Electric propulsion plants do require to be powered by on-board generators, battery banks or energy storage systems. This may drive weight shipboard back up and eliminate any savings thanks to the disposal of any reduction and reversing gears. However, electric propulsion accommodates substantial flexibility e.g. regarding the on-board location of the power generation sets (engine-generator) as well as thrusters. The thruster prime movers and power generation sets can be located on the same or opposite sides or ends of a vessel since the only requirement is to link them through power transmission lines or cables.

Selection of parts for our marine propulsion plant model paradigm was made based on a thorough survey of marine engineering practices, data and information available. The marine propulsion plant in our actual numerical simulations includes two identical powertrains one on the port and one on the starboard side of the craft. Each powertrain consists of a 3-phase induction motor, transmission shaft-line without any gearing, and a surface-piercing propeller as well as a PID speed governor and an empirical phenomenological model for the planing-hull processes.

2. Alternative Propulsion Plant Modelling

The alternative marine propulsion plant model was outfitted in MATLAB/Simulink using blocks. The propulsion plant is outfitted with an alternative prime mover. The commonplace choice of prime mover for both planing-hull and displacement vessels is an internal combustion engine, in-board or outboard, with possibly a gearbox system coupling it with a fully submerged propeller (Figure 1). In our case, however, the prime mover is an electric motor which is connected directly with a surface-piercing propeller (Figure 2) [4]. Configuration specifics for the planing hull under consideration are provided in Appendix A.

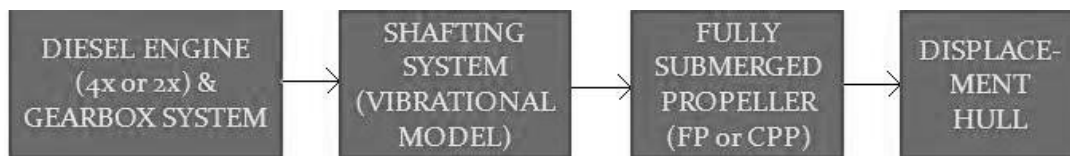


Figure 1. Conventional marine propulsion plant.

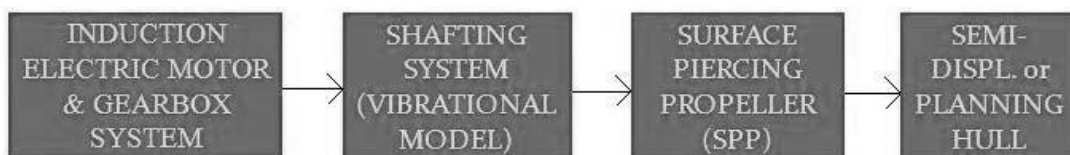


Figure 2. Alternative marine propulsion plant.

The dynamical model is presented below for each part of such alternative propulsion plant.

2.1. Prime Mover Modelling

2.1.1. 3-Phase Induction Alternating Current (AC) Motor Block

The workhorse in industrial applications for motion control is no other than alternating current (AC) induction motors. The main advantages of this motor type are that it is simple and rugged, with minimal requirements in terms of cost and maintenance, and amenable to hookup straight to standard AC. Until recently, speed control of induction motors, however, was rather hard. This is why they were mainly employed in constant rpm applications used at constant speed. In some cases where electric propulsion was employed with induction motors, the motor was running at constant speed and the propulsion powertrain was in result outfitted with a controllable pitch propeller to adjust and vary thrust at will in real time. Relatively recent progress in solid-state switching control drove the cost down and improved efficiency of variable speed drives for induction motors. Such progress lead to the point where employing of synchronous or induction motors with variable speed control drives

has become ubiquitous. Progress in technology of variable speed AC and in specific induction motors gives them a substantial advantage when compared to direct current (DC) machinery. Among some of the reasons is that AC machines are more efficient at least when operating as motors; they also require less maintenance than DC machinery since brushes or other commutation devices are done away with; finally, they are less bulky and lighter machines for comparable power output.

The SimPowerSystems toolbox comes as an extension of standard MATLAB/Simulink. It is a comprehensive library with dynamic models including for 3-phase induction motors. In specific, there is a block to model and simulate a generic 3-phase squirrel-cage induction machine. A prominent feature of this library is that any piece of machinery can run either as generator or as motor. Mode of operation is determined by adjusting the sign of external load torque T_m . If positive, the machine runs as motor, and if negative as generator or dynamic brake, i.e. energy recovery device.

The modeling theory behind SimPowerSystems is the standard DQ/dq model shown in Figure 3 [5]. In the toolbox it is implemented as a fourth-order, state-space model, the dynamical system of the machine is split to an electrical part while a second-order subsystem implements the dynamics of the mechanical part. For a typical squirrel-cage induction motor, the toolbox includes a set of predefined electrical and mechanical parameters for a broad spectrum of power ratings, phase-to-phase voltage, rpm and frequency values.

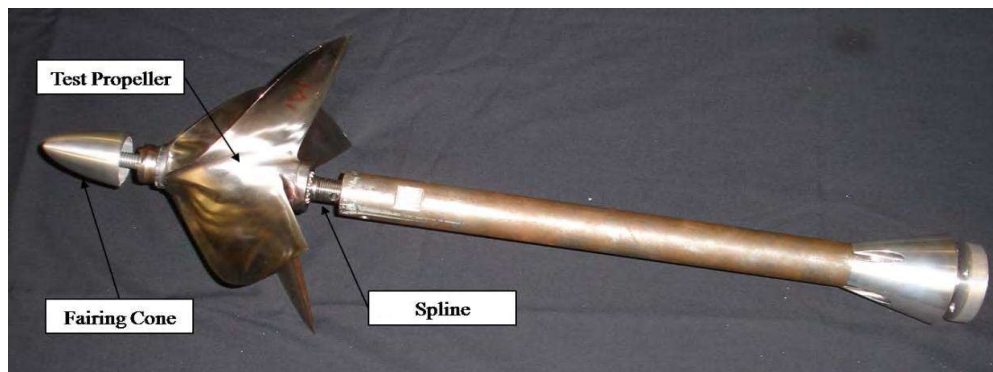


Figure 3. Test propeller with shaft assembly.

For the induction machine model to run, the user needs to define an external mechanical torque as load. In our case the torque of the SPP is employed as load. The motor block internally computes the rotor speed by dividing the torque difference, external load torque load T_m of the propeller minus electromagnetic torque T_e developed by the motor, with the total system inertia.

The section below provides the numerical approach used to model the induction motor. The simulation model was built in MATLAB/Simulink using the induction machine toolbox (SimPowerSystem library) as already outlined. The induction machine model (Equations (1)–(4)) consists of two modules: flux and current model (FCM) and electromagnetic torque model (EMTM), as shown in Figure 4.

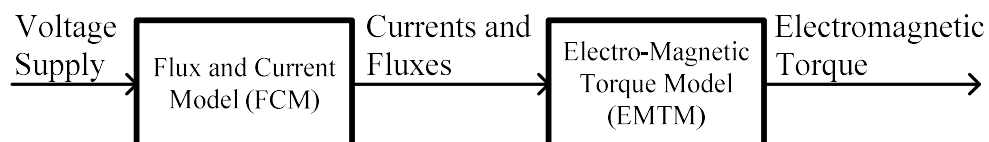


Figure 4. Block diagram of the 3 phase alternating current (AC) induction motor model.

The FCM solves the induction motor voltage equations, taking into account a stator reference frame. The direct-quadrature or d-q equivalent circuit is used; specifically, d-q transformation is employed in order to simplify the analysis of three-phase circuits. The electrical circuit diagram of the FCM model is given in Figure 5.

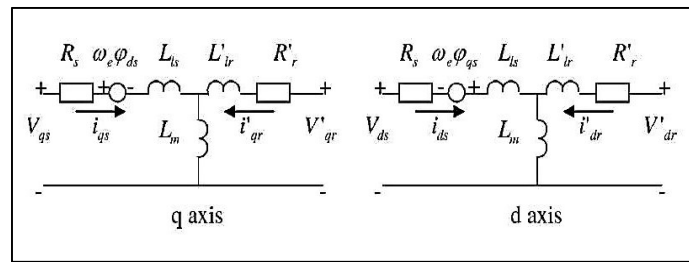


Figure 5. Circuit equivalent model of the squirrel cage induction generator (flux and current model (FCM)).

The equations describing the voltages of the FCM for stator and rotor are the following:

$$V_{qs} = R_s \cdot i_{qs} + \frac{d\varphi_{qs}}{dt} + \omega_s \cdot \varphi_{ds} \tag{1}$$

$$V_{ds} = R_s \cdot i_{ds} + \frac{d\varphi_{ds}}{dt} - \omega_s \cdot \varphi_{qs} \tag{2}$$

$$V_{qr} = R_r \cdot i_{qr} + \frac{d\varphi_{qr}}{dt} + (\omega_s - \omega_r) \cdot \varphi_{dr} \tag{3}$$

$$V_{dr} = R_r \cdot i_{dr} + \frac{d\varphi_{dr}}{dt} - (\omega_s - \omega_r) \cdot \varphi_{qr} \tag{4}$$

In these equations the corresponding flux variables can be calculated according to:

$$\varphi_{qs} = L_s \cdot i_{qs} + L_m \cdot i_{qr} \tag{5}$$

$$\varphi_{ds} = L_s \cdot i_{ds} + L_m \cdot i_{dr} \tag{6}$$

$$\varphi_{qr} = L_r \cdot i_{qr} + L_m \cdot i_{qs} \tag{7}$$

$$\varphi_{dr} = L_r \cdot i_{dr} + L_m \cdot i_{ds} \tag{8}$$

The inductance values in the above equations are given by:

$$L_s = L_{ls} + L_m \tag{9}$$

$$L_r = L_{lr} + L_m \tag{10}$$

In these equations $R, L, \omega, V, i,$ and φ denote resistance, inductance, electrical frequency, voltage, current, and flux respectively, referring to rotor (subscript r) and stator (subscript s) on the d-q axes.

Solving for stator and rotor current from Equations (5)–(8) yields:

$$i_{qr} = \frac{\varphi_{qs} - L_s \cdot i_{qs}}{L_m} \tag{11}$$

$$i_{dr} = \frac{\varphi_{ds} - L_s \cdot i_{ds}}{L_m} \tag{12}$$

$$i_{qs} = \frac{\varphi_{qr} - L_r \cdot i_{qr}}{L_m} \tag{13}$$

$$i_{dr} = \frac{\varphi_{dr} - L_r \cdot i_{dr}}{L_m} \tag{14}$$

Substituting Equations (11) and (12) into (13) and (14) respectively yields:

$$i_{qs} = \frac{L_m \cdot \varphi_{qr} - L_r \cdot \varphi_{qs}}{L_m^2 - L_r \cdot L_s} \tag{15}$$

$$i_{ds} = \frac{L_m \cdot \varphi_{dr} - L_r \cdot \varphi_{ds}}{L_m^2 - L_r \cdot L_s} \tag{16}$$

and similarly Equations (15) and (16) into (11) and (12) respectively yields:

$$i_{qr} = \frac{L_m \cdot \varphi_{qs} - L_s \cdot \varphi_{qr}}{L_m^2 - L_r \cdot L_s} \tag{17}$$

$$i_{dr} = \frac{L_m \cdot \varphi_{ds} - L_s \cdot \varphi_{dr}}{L_m^2 - L_r \cdot L_s} \tag{18}$$

Given that the 3-phase motor voltages are balanced, the q and d-axis rotor voltages, V_{qr} and V_{dr} respectively can be assumed to be zero. By substituting stator and rotor currents from Equations (15)–(18) back to Equations (1)–(4) it is finally derived that:

$$\frac{d\varphi_{qs}}{dt} = V_{qs} - R_s \cdot \left(\frac{L_m \cdot \varphi_{qr} - L_r \cdot \varphi_{qs}}{L_m^2 - L_r \cdot L_s} \right) - \omega_s \cdot \varphi_{ds} \tag{19}$$

$$\frac{d\varphi_{ds}}{dt} = V_{ds} - R_s \cdot \left(\frac{L_m \cdot \varphi_{dr} - L_r \cdot \varphi_{ds}}{L_m^2 - L_r \cdot L_s} \right) + \omega_s \cdot \varphi_{qs} \tag{20}$$

$$\frac{d\varphi_{qr}}{dt} = -R_r \cdot \left(\frac{L_m \cdot \varphi_{qs} - L_s \cdot \varphi_{qr}}{L_m^2 - L_r \cdot L_s} \right) - (\omega_s - \omega_r) \cdot \varphi_{dr} \tag{21}$$

$$\frac{d\varphi_{dr}}{dt} = -R_r \cdot \left(\frac{L_m \cdot \varphi_{ds} - L_s \cdot \varphi_{dr}}{L_m^2 - L_r \cdot L_s} \right) + (\omega_s - \omega_r) \cdot \varphi_{qr} \tag{22}$$

The EMTM computes electromagnetic torque, T_e , employing flux and current values of the stator according to the following:

$$T_e = 1.5 \cdot p \cdot (\varphi_{ds} \cdot i_{qs} - \varphi_{qs} \cdot i_{ds}) \tag{23}$$

where p is the number of pole pairs. Substituting stator currents (Equations (15) and (16)) in Equation (23), electromagnetic torque is expressed as a function solely of flux variables. This is convenient because flux variables can be obtained by the four first-order coupled differential Equations (19)–(22).

$$T_e = 1.5 \cdot p \cdot \left(\varphi_{ds} \cdot \frac{L_m \cdot \varphi_{qr} - L_r \cdot \varphi_{qs}}{L_m^2 - L_r \cdot L_s} - \varphi_{qs} \cdot \frac{L_m \cdot \varphi_{dr} - L_r \cdot \varphi_{ds}}{L_m^2 - L_r \cdot L_s} \right) \tag{24}$$

The dynamic model derived is a system of four first-order coupled differential Equations (19)–(22), and along with electromagnetic torque (Equation (24)) constitutes a system with five unknowns and five equations, depending solely on d-q voltages.

The motor’s electromagnetic torque, along with the mechanical torque load, T_m (see Section 2.3) on the shaft, can then be used in the equation of motion to compute rotational acceleration and speed of the rotor.

$$\dot{\omega}_r = \frac{(T_e - F \cdot \omega_r - T_m)}{2 \cdot H} \tag{25}$$

$$\omega_r = \omega_r(t=0) + \int_0^t \dot{\omega}_r dt \tag{26}$$

where ω_r is the rotor’s angular speed (rpm), H the joint load (i.e. propeller) and rotor inertia and F is the combined load (propeller) and viscous friction coefficient.

The (mechanical angular) synchronous speed, ω_s , is given by the following equation:

$$\omega_s = \frac{2 \cdot \pi \cdot f}{p} \tag{27}$$

where f stands for the electrical (AC) frequency in Hz.

The 3-phase induction motor characteristics implemented in this model are shown in Table 1.

Table 1. Induction motor parameters.

AC Induction Motor Parameters 50 kW, 460 V(rms), 145 Hz, 4350 rpm, Squirrel Cage Rotor	
Stator Resistance (R_s)	0.0641 Ω
Rotor Resistance (R_r)	0.0441 Ω
Magnetizing Inductance (L_m)	0.0100644 H
Total (Rotor & Stator) Inductance ($L_{ls} + L_{lr}$)	0.0006449 H
Total Moment of Inertia (H)	0.35 kg·m ²
Friction Factor (F)	0.0025 N·m·s
Number of Pole Pairs (p)	2

2.1.2. Proportional-Integral-Derivative (PID) Block and PID Controller Tuning

A PID (proportional-integral-derivative) controller is employed for the speed governor action i.e., for rpm regulation of the system. By design, it monitors the actual rotational speed of the shaft through a speed sensor such as an optical encoder or Hall-effect sensor. The controller compares the value to the one of the setpoint (reference) rotational speeds provided by the human operator of the system. Employing the difference (error) between these two values, the controller then generates a control signal to adjust the motor drive’s frequency. This adjustment is then superimposed onto the offset frequency of the electrical drive and finally fed to the machine’s electrical signal as per the speed-frequency cross-reference (lookup) table. The 2D speed-frequency lookup table is used to convert a setting for the rotational speed of the electric motor to a pulse frequency (drive frequency). The adjustment issued by the controller is superimposed as shown in Figure 6.

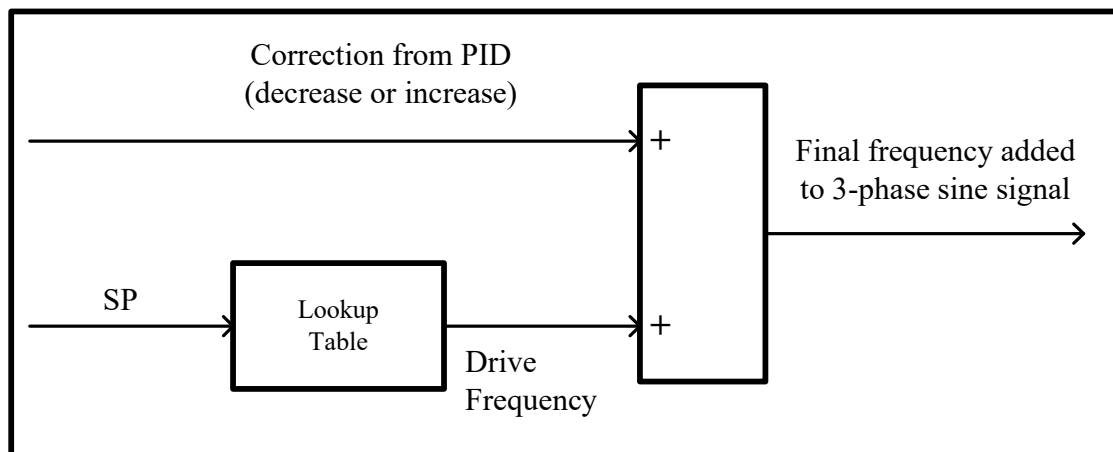


Figure 6. Rotational speed-drive frequency lookup table and proportional-integral-derivative (PID) perturbation.

The PID controller is tuned to reduce deviation arising in torque and rotational speed. A tuning method by Ziegler and Nichols was employed to determine the gain values of the controller: K_I , K_P and K_D . Integral and derivative gain are set initially to zero while the proportional gain is gradually increased until an oscillation of the regulated variable (rotational speed) is traced in the response. Once detected, the proportional gain value is recorded as the ultimate value K_u as well as the period of oscillations, T_u . Finally K_P and K_I are determined using the following:

$$K_p = 0.6 \cdot K_u \tag{28}$$

$$K_I = (1.2 \cdot K_u) / T_u \tag{29}$$

$$K_D = 0.075 \cdot K_u \cdot T_u \tag{30}$$

In our case the setpoint (SP) is the required speed of electric motor (rotor), the process variable (PV) is the actual value of rotor speed, the process block is the electric motor and the manipulated variable (MV) is the adjustment of the drive’s frequency as shown in Figure 7.

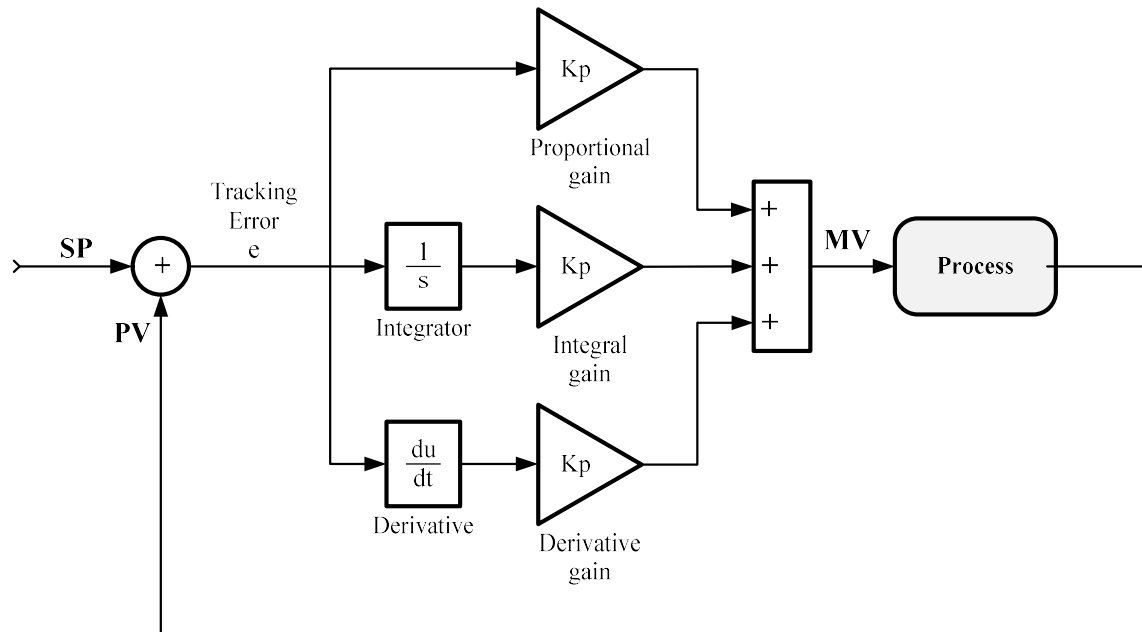


Figure 7. General form of the PID controller.

The values for the gain parameters are shown in Table 2. The D gain in the PID controller is intentionally set to zero to avoid high-frequency noise components in MV that can lead to problematic jiggling and fluctuation of the electric motor’s torque. The inertia of the propeller also attenuates oscillations so there seems to be no need for additional dynamic terms that may complicate tuning. This is the main reason why full PID, three-term control is only scarcely used in applied practice; especially for rotational speed control of electric motors, PI controllers (with zero D-term) are the predominant option of choice.

Table 2. Controller gains.

PID Gain	Value
K_P	0.001
K_I	0.015
K_D	0.000

2.2. Propulsor Modelling

2.2.1. Towing Tank Data for Surface-Piercing Propeller

A train of towing tank experiments were performed on a SPP manufactured by at Stevens Institute of Technology in New Jersey in collaboration with Florida Atlantic University. The towing tank test settings are specified in Table 3.

Table 3. Test condition settings of surface-piercing propeller (SPP).

Immersion Ratio I_T (%)	Pitch Angle γ (Degrees) (Shaft Inclination Angle)	Yaw Angle ψ (Degrees)	Advance Ratio J (-)
33	0, 7.5, 15	0, 15, 30	$0.8 \div 1.9$
50	0	0	$0.8 \div 1.9$

The immersion and advance ratio are defined as:

$$I_T = \frac{h}{D_p} \tag{31}$$

$$J = \frac{U_A}{n * D_p} \tag{32}$$

where h is the distance from bottom tip of propeller to free surface, D stands for propeller diameter, n is the rotational rate of the propeller and U_A is the advance velocity.

The characteristics of the propeller are shown in Table 4.

Table 4. SPP characteristics.

Characteristic Type	Characteristic Value
Rotation	Left Handed
Pitch (P)	0.465 m
Bore	Splined
Diameter (D_p)	0.2464 m
Number of Blades (z)	4
Material	Stainless Steel
Number of Propellers (N_p)	2

Several issues occurred with thrust and torque measurement when the test data of the initial phase were analyzed by Justin M. Lorio. The measurement results were obtained by time averaging. Forces on the propeller were recorded while inclination angle, yaw angle and immersion depth were changed over a broad range of advance ratio. As can be seen, in the beginning measured thrust grows rapidly to its maximum since the propeller is accelerating faster than the carriage. Effectively, the carriage is dragged by the propeller. But as the carriage and the propeller reach steady-state, thrust gradually shrinks until it stabilizes. As soon as data time series were collected, Lorio observed that non-negligible interference was developing when thrust and torque were measured simultaneously [2,4]. The measured values for torque were found to be 10% lower than predicted whereas thrust required more investigation. As thrust approached steady-state, it actually became negative. The issue was resolved by incorporating a thrust bias in the system. Then, when time averaging thrust force is achieved, the bias was applied to the raw data, yielding positive values. The method was refined and realized in the resulting coefficients of thrust included in his thesis, where the reader can find more details.

2.2.2. Configuration of Artificial Neural Networks (ANN)

The artificial neural networks (ANN) for calculation of a surface-piercing propeller’s thrust and torque are implemented in MATLAB using Neural Network Toolbox functions. The command(s) employed *newff* in later versions and *feedforwardnet* in newer versions of MATLAB. This command creates a feedforward neural network which consists of a series of layers. The first layer has a connection from the network input. Each subsequent layer has a connection from the previous layer. The final layer produces the network’s output.

The inputs in our case are five and are conveniently packed in vector $\vec{\xi}$:

$$\vec{\xi} = (I_T; \gamma; \psi; n; U_A) \quad (33)$$

Moreover, the commands *init* and *train* are used for training neural networks. The command *init* returns a newly created, yet untrained, neural network with weight and bias values updated according to the network initialization function and the settings. The command *train* trains such neural network according to data series available, and gives such as number of hidden layers, neurons etc., and the training function (see Sections 2.2.3 and 2.2.4). In the present work, the transfer function for both neural networks is the Logistic-Sigmoid (*logsig* in MATLAB) defined below:

$$\varphi_{\text{logsig}}(x) = \frac{1}{1 + e^{-x}} \quad (34)$$

which can have any value between plus and minus infinity ($-\infty < x < +\infty$), and squashes the output into the range 0 to 1.

The output values produced by an ideal neural net would coincide in full with the measurements. Practically, however, it is only possible to assess the accuracy of the simulated torque and thrust neural networks by applying linear regression to see how well the network outputs converge toward the corresponding target values.

After training the ANNs, those that produce the most promising output were saved to be used as a mathematical expression in Simulink. The basis of determining a promising network is the comparison of actual test data (experimental data or training data) to the output of the net (simulated data). Linear regression analysis of the neural net gives a correlation coefficient value R of 98% for the thrust (see Figure 8) ($R = 1$ indicates a perfect match) and 96% for the torque (see Figure 9). These networks provided the best fit and were employed to predict the dynamic variables of the SPP at any I_T , ψ , γ and J .

As will be seen the thrust and torque neural nets share the same feedforward architecture structured in layers with one output and one input layer. Both nets produce a scalar output and have one neuron in the output layer. However, the number of layers was chosen so optimal performance could be achieved with the minimal number of hidden layers and neurons; as a result, by trial and error it was determined to be different and specific for each network.

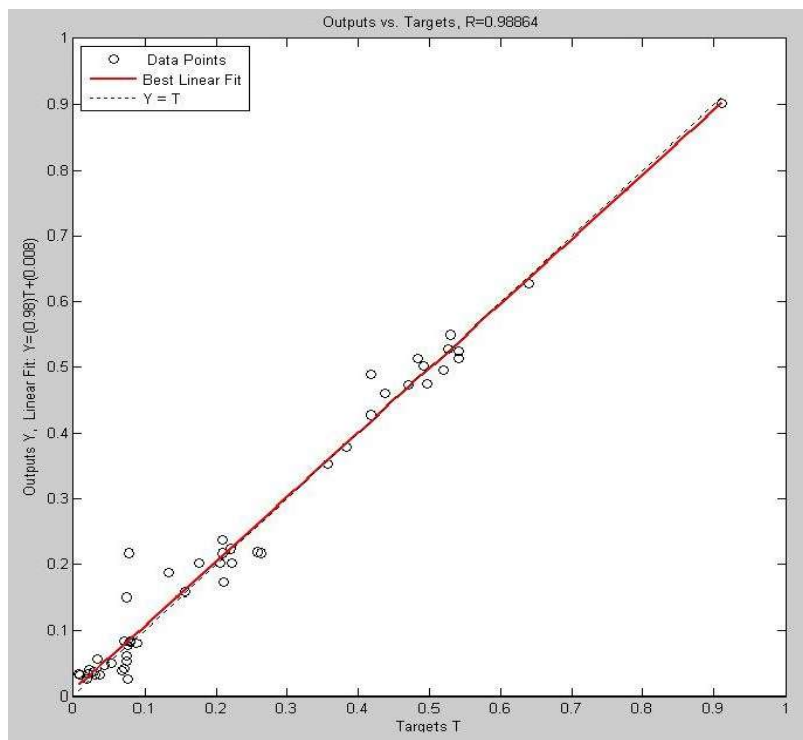


Figure 8. Thrust neural network regression. analysis (outputs vs. targets).

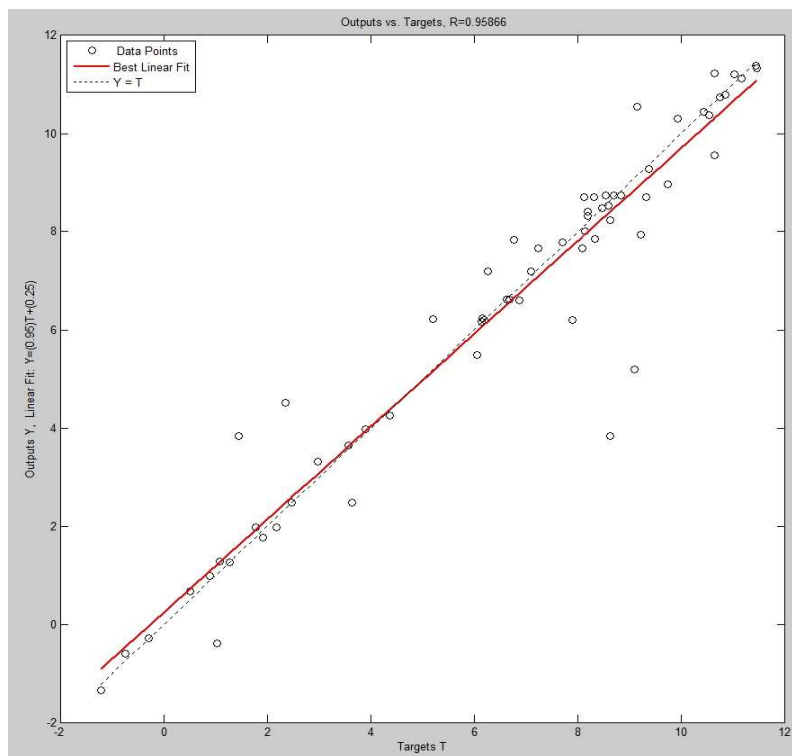


Figure 9. Torque neural network regression. analysis (outputs vs. targets).

2.2.3. Thrust ANN

A feed-forward artificial neural network was developed where the experimental data from the surface-piercing propeller are reproduced by the trained network. The internal structure of the thrust neural network is shown in Figure 10.

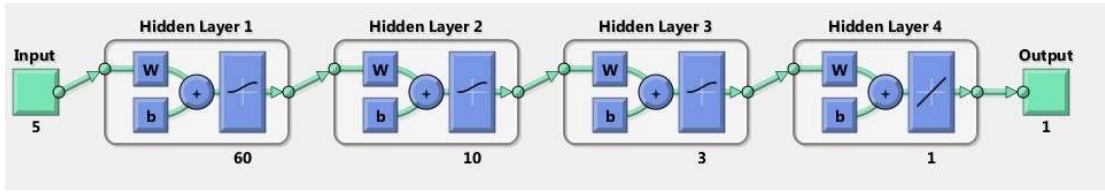


Figure 10. Thrust neural network topology.

The characteristics of the thrust neural network are the following:

- Four layers;
- (60, 10, 3, 1) where 60 are the neurons of the 1st layer, 10 the neurons of the 2nd layer, 3 of the 3rd layer and 1 the number of neurons of the 4th;
- The transfer function for the first three layers is Logistic-Sigmoid (*logsig*) and pure linear for the last layer;
- The training function was selected as Conjugate Gradient Back-Propagation with Polak-Ribiere Updates (*traincgp*);
- The number of inputs are 5 ($\vec{\xi}$) and number of outputs is 1 (Thrust: T_{SPP}).

$$\vec{r}_{HL1T} = \varphi_{logsig}(\overleftrightarrow{\mathbf{W}}_{1T} \cdot \vec{\xi} + \vec{\mathbf{b}}_{1T}) \tag{35}$$

$$\vec{r}_{HL2T} = \varphi_{logsig}(\overleftrightarrow{\mathbf{W}}_{2,1T} \cdot \vec{r}_{HL1T} + \vec{\mathbf{b}}_{2T}) \tag{36}$$

$$\vec{r}_{HL3T} = \varphi_{logsig}(\overleftrightarrow{\mathbf{W}}_{3,2T} \cdot \vec{r}_{HL2T} + \vec{\mathbf{b}}_{3T}) \tag{37}$$

$$T_{SPP} = \overleftrightarrow{\mathbf{W}}_{4,3T} \cdot \vec{r}_{HL3T} + \vec{\mathbf{b}}_{4T} \tag{38}$$

where \vec{r}_{HL1T} , \vec{r}_{HL2T} , \vec{r}_{HL3T} are the results/output of Hidden Layer 1, 2 and 3 respectively, $\vec{\mathbf{b}}_{1T}$, $\vec{\mathbf{b}}_{2T}$, $\vec{\mathbf{b}}_{3T}$, $\vec{\mathbf{b}}_{4T}$ are the bias vectors of Layer 1, 2, 3 and 4 respectively, matrix $\overleftrightarrow{\mathbf{W}}_{1T}$ hold the weights of Layer 1, matrices $\overleftrightarrow{\mathbf{W}}_{2,1T}$, $\overleftrightarrow{\mathbf{W}}_{3,2T}$, $\overleftrightarrow{\mathbf{W}}_{4,3T}$ hold the weights for Layer 2, 3 and 4 respectively. Subscript T stands for thrust neural network. Finally, T_{SPP} is the thrust estimate for the surface-piercing propeller produced by the net (output of Layer 4).

2.2.4. Torque ANN

A feed-forward artificial neural network was developed where the experimental data from the surface-piercing propeller are reproduced by the trained network. The schematic diagram of the topology of the neural network is shown in Figure 11.

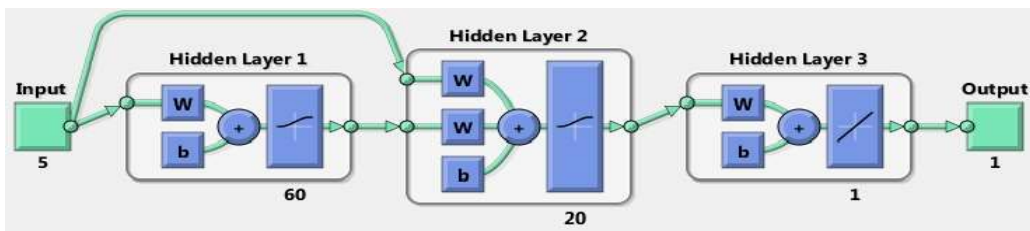


Figure 11. Torque neural network topology.

The characteristics of the torque neural network are the following:

- Three (3) layers;
- (60, 20, 1) where 60 are the neurons of the 1st layer, 20 the neurons of the 2nd layer and 1 the number of neurons of the 3rd;

- The transfer function for the first two layers is Logistic-Sigmoid (*logsig*) and pure linear (*purelin*) for the last layer;
- The training function was selected as Conjugate Gradient Back-Propagation with Polak–Ribiere Updates (*traincgp*);
- The number of inputs are 5 ($\vec{\xi}$) and number of outputs is 1 (Torque: Q_{SPP}).

$$\vec{r}_{HL1Q} = \varphi_{logsig}(\overleftrightarrow{W}_{1Q} \cdot \vec{\xi} + \vec{b}_{1Q}) \tag{39}$$

$$\vec{r}_{HL2Q} = \varphi_{logsig}(\overleftrightarrow{W}_{2Q} \cdot \vec{\xi} + \overleftrightarrow{W}_{2,1Q} \cdot \vec{r}_{HL1Q} + \vec{b}_{2Q}) \tag{40}$$

$$Q_{SPP} = \overleftrightarrow{W}_{3,2Q} \cdot \vec{r}_{HL2Q} + \vec{b}_{3Q} \tag{41}$$

where \vec{r}_{HL1Q} , \vec{r}_{HL2Q} are the results of Layer 1 and 2 respectively, \vec{b}_{1Q} , \vec{b}_{2Q} , \vec{b}_{3Q} are the bias vectors of Layer 1, 2 and 3 respectively, matrices $\overleftrightarrow{W}_{1Q}$, $\overleftrightarrow{W}_{2Q}$ hold the external input weights of Layer 1 and 2 respectively, matrices $\overleftrightarrow{W}_{2,1Q}$, $\overleftrightarrow{W}_{3,2Q}$ hold the intermediate weights of Layer 2 and 3 respectively. Subscript Q stands for torque neural network. Finally, Q_{SPP} is the torque estimate for the surface-piercing propeller produced by the net (output of Layer 3).

The size of weight matrices, bias vector and layer output vector for each one of the two neural networks are summarized in Table 5.

Table 5. Size of weight matrices, bias. vectors and hidden layers outputs.

Matrix or Vector	Size
$\overleftrightarrow{W}_{1T}$	(60×5)
$\overleftrightarrow{W}_{2,1T}$	(10×60)
$\overleftrightarrow{W}_{3,2T}$	(3×10)
$\overleftrightarrow{W}_{4,3T}$	(1×3)
\vec{b}_{1T}	(60×1)
\vec{b}_{2T}	(10×1)
\vec{b}_{3T}	(3×1)
\vec{b}_{4T}	(1×1)
\vec{r}_{HL1T}	(60×1)
\vec{r}_{HL2T}	(10×1)
\vec{r}_{HL3T}	(3×1)
$\overleftrightarrow{W}_{1Q}$	(60×5)
$\overleftrightarrow{W}_{2Q}$	(20×5)
$\overleftrightarrow{W}_{2,1Q}$	(20×60)
$\overleftrightarrow{W}_{3,2Q}$	(20×1)
\vec{b}_{1Q}	(60×1)
\vec{b}_{2Q}	(20×1)
\vec{b}_{3Q}	(1×1)
\vec{r}_{HL1Q}	(60×1)
\vec{r}_{HL2Q}	(20×1)

2.3. Propulsion Shaft Vibrational Modelling

The propulsion shaft model consists of a cascaded rectilinear interconnection of inertial masses and torsional springs with friction losses on the inertial elements. The inputs to the shafting are applied

on the two ends of the shaft line and they are both time dependent. On one end is the prime mover’s torque and on the other end the propeller torque.

An 1D (one-dimensional) dynamical system comprising torsional springs, inertias and support bearings with friction is used to model the propeller shaft dynamics. The structure of this model is shown in the schematic of Figure 12.

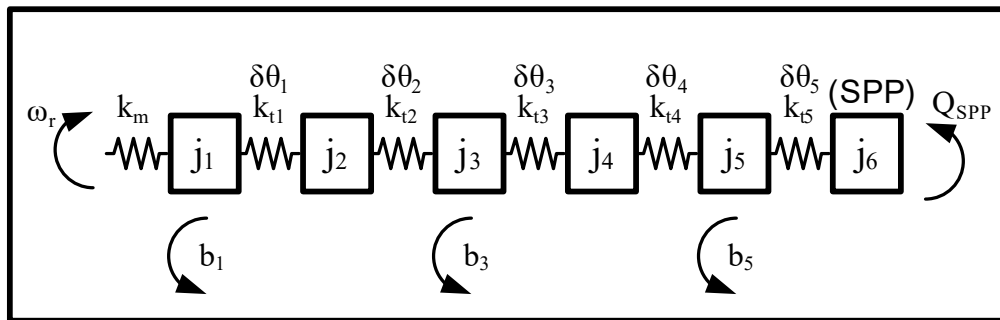


Figure 12. Shafting vibrational model mechanical system.

A theoretical investigation of the shaft and the propeller yields the natural frequencies of the system [6]. Then, the propeller shaft diameter as well as its material is configured so that the natural frequencies of both components are placed in an admissible range in the vicinity of double its frequency of resonance [6]. The hollow-type shaft has a length of 2 m and supported by three bearings located one after the electric motor flange, one midway along the shaft line, and one before the propeller (SPP) mount. The system is modeled as a rectilinear arrangement of six elements. Some additional data for the shafting system are given in Table 6.

Table 6. Propulsion shaft characteristics.

Shaft Characteristic	Value
Shaft Length	2 m
Number of Elements	6 (-) (Propeller + 5 elements)
Number of Springs	6 (-)
Shaft Diameter (Hollow Type)	D_{out} : 8 cm (outer) D_{in} : 5 cm (inner)
Shaft-Primer Mover Flange	D_f : 15 cm l_f : 5 cm
Number of Bearings	3 (-)
Shaft Material	Stainless Steel

Beyond the geometry and the construction material of the propulsion shaft, the vibrational investigation model also requires knowledge of the shear modulus and the density of the shaft’s material, the inertial values of the propulsor (j_p) and shaft elements (j_i), the friction coefficients of the support bearings (b_i) and the torsion spring coefficients (k_{ti}).

The vibrational investigation model of the shafts receives a torque load from the surface-piercing propeller which is the resistance torque developed by the propeller during operation (Q_{SPP}). The other input to the shaft model is the rotational speed (ω_r) of the prime mover which in our case is the AC induction motor.

The shaft model generates the load torque value applied to the induction motor (T_m) and the rotational speed (n) of the SPP as shown in Figure 13.

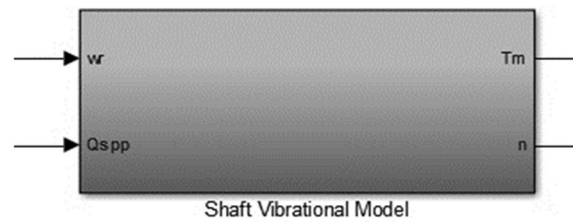


Figure 13. Inputs (left) and outputs (right) for the block. Implementing the shafting vibrational model in MATLAB/Simulink.

The differential equations representing the dynamic behavior of the system are as follows:

$$\frac{d\vec{\omega}}{dt} = \overset{\leftrightarrow}{J} \cdot \vec{T} + \overset{\leftrightarrow}{K_t} \cdot \vec{\delta\theta} - \overset{\leftrightarrow}{B} \cdot \vec{\omega} \tag{42}$$

where $\overset{\leftrightarrow}{K_t}$ is the shaft stiffness matrix (6×5), $\overset{\leftrightarrow}{J}$ is the matrix holding the moments of inertia (6×2), $\overset{\leftrightarrow}{B}$ is the matrix holding the friction coefficients (6×6), $\vec{\delta\theta}$ is the vector holding deformation variables of the shaft elements (5×1), $\vec{\omega}$ is the shaft rotational speed vector (6×1) and \vec{T} is the torque vector (2×1). The afore mentioned vectors and matrices are defined using the following equations:

$$\overset{\leftrightarrow}{K_t} = \begin{bmatrix} k_{t1}/j_1 & 0 & 0 & 0 & 0 \\ -k_{t1}/j_2 & k_{t2}/j_2 & 0 & 0 & 0 \\ 0 & -k_{t2}/j_3 & k_{t3}/j_3 & 0 & 0 \\ 0 & 0 & -k_{t3}/j_4 & k_{t4}/j_4 & 0 \\ 0 & 0 & 0 & -k_{t4}/j_5 & k_{t5}/j_5 \\ 0 & 0 & 0 & 0 & -k_{t5}/j_p \end{bmatrix}, \vec{\delta\theta} = \begin{bmatrix} \delta\theta_1 \\ \delta\theta_2 \\ \delta\theta_3 \\ \delta\theta_4 \\ \delta\theta_5 \end{bmatrix} \tag{43}$$

$$\overset{\leftrightarrow}{B} = \begin{bmatrix} b_1/j_1 & 0 & 0 & 0 & 0 & 0 \\ 0 & 0 & 0 & 0 & 0 & 0 \\ 0 & 0 & b_3/j_3 & 0 & 0 & 0 \\ 0 & 0 & 0 & 0 & 0 & 0 \\ 0 & 0 & 0 & 0 & b_5/j_5 & 0 \\ 0 & 0 & 0 & 0 & 0 & 0 \end{bmatrix}, \vec{\omega} = \begin{bmatrix} \omega_1 \\ \omega_2 \\ \omega_3 \\ \omega_4 \\ \omega_5 \\ \omega_6 \end{bmatrix} \tag{44}$$

$$\overset{\leftrightarrow}{J} = \begin{bmatrix} 1/j_1 & 0 \\ 0 & 0 \\ 0 & 0 \\ 0 & 0 \\ 0 & 0 \\ 0 & -1/j_p \end{bmatrix}, \vec{T} = \begin{bmatrix} T_m \\ Q_{SPP} \end{bmatrix} \tag{45}$$

where b_1, b_2, b_3 are the viscous friction coefficients at the support points, j_1, j_2, j_3, j_4, j_5 are the moments of inertia of the shaft elements and j_p is the moment of inertia of propeller, $k_{t1}, k_{t2}, k_{t3}, k_{t4}, k_{t5}$ are the torsional spring constants, $\delta\theta_1, \delta\theta_2, \delta\theta_3, \delta\theta_4, \delta\theta_5$ are the deformation angles of shaft torsional springs, $\omega_1, \omega_2, \omega_3, \omega_4, \omega_5$ are the angular velocities of shaft elements and ω_6 is the rotational velocity of propeller.

The load torque applied to the motor is given by the following equation:

$$T_m = k_m \cdot \delta\theta = k_m \cdot (\theta_r - \theta_1) = k_m \cdot \int (\omega_r - \omega_1) dt \tag{46}$$

and the rotational speed of the surface-piercing propeller is derived from the following equation:

$$n \text{ (rps)} = \frac{\omega_6}{2 \cdot \pi} \tag{47}$$

The value of torsional coefficient k_m , which refers to the spring that connecting the electric motor flange with the first shaft element, depends on flange geometry as in the expression below:

$$k_m = \frac{G \cdot j_m}{l_f} \tag{48}$$

$$j_m = \frac{1}{32} \cdot \pi \cdot (D_f^4) \tag{49}$$

where l_f, D_f are the length and the diameter of electric motor flange respectively and j_m is the flange's polar moment of inertia.

For shafts of hollow type with a cross-section that is circular and uniform, moment of inertia and stiffness are given by the following equations:

$$k_{ti} = \frac{G \cdot j_{polar,i}}{l_i} \tag{50}$$

$$j_{polar,i} = \frac{1}{32} \cdot \pi \cdot (D_{out}^4 - D_{in}^4) \tag{51}$$

$$j_i = \frac{1}{8} \cdot m_i \cdot (D_{out}^2 + D_{in}^2) \tag{52}$$

$$m_i = \rho \cdot l_i \cdot \pi \cdot \left(\left(\frac{D_{out}}{2} \right)^2 - \left(\frac{D_{in}}{2} \right)^2 \right) \tag{53}$$

where $i = 1, 2, 3, 4, 5$ is the number of shaft elements, j_{polar} is the polar inertia moment of each shaft element, m is the mass, ρ is the material density, G the material's shear modulus or modulus of elasticity and l is the length of each shaft element; in our analysis, each element's length is 0.4 m.

The advanced theoretical and numerical background involved in bearing viscous friction lies beyond the scope of this investigation. For practical analysis purposes as common in marine engineering and applied research, an empirical damping coefficient is used to model viscous frictional losses; in this case a typical and reasonable value of such damping coefficient for all three bearings (b_1, b_2 and b_3) is 0.00825 N·m·s/rad. The resulting shaft model is also shown in Figure 14.

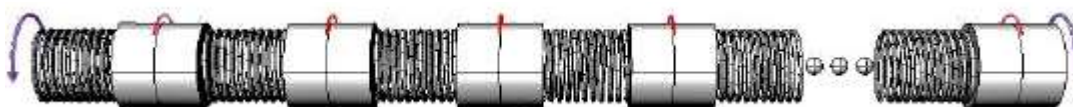


Figure 14. Representation of the propulsion shaft as a discretized cascaded 1D interconnection of inertial mass and spring elements.

The time step for the shaft model is selected according to its resonance frequency and the number of elements. In specific, the number of samples per second in the model needs to be at least double (Nyquist rate) the mechanical resonance frequency, $(k/m)^{1/2}$, of the shaft times the number of cells (five in our analysis). This is typical a fraction of one degree of rotation, increasing the computational requirement significantly.

2.4. Equation for Linear Longitudinal Motion (Surge Dynamics)

The surge dynamics of a vessel can be approximated by the following equation [7,8]:

$$\sum Force = \Delta \cdot \frac{dV_s}{dt} \Leftrightarrow T_{SPP} \cdot (1-t) \cdot p - D = \Delta \cdot \frac{dV_s}{dt} \tag{54}$$

The value for T_{SPP} above comes from the ANN for SPP torque, the displacement of the planing watercraft (Δ) is 795 kg; the effect of added masses has been neglected as is common practice for this size and type of watercraft. The resistance drag (D) in the equation above is calculated according to Savitsky General Case Method (Savitsky, 1964) with a script programmed in MATLAB. The hull characteristics in Table 7 were used and the range of speeds is 0 to 43 knots (23.121 m/s).

Table 7. Hull characteristics.

Hull Characteristic	Value
L_{OA}	5.28 m
B_{chine}	2.11 m
Deadrise (β)	19°
Displacement (Δ)	795 kg
LCG/VCG	2.398 m/0.316 m
Inclination of Thrust Line Relative to Keel (e)	0°

Employing Savitsky general case method [7,8], the so called “equilibrium trim” τ_e (trim of the planing craft when she is in equilibrium conditions, summary of pitching moments is zero, at a given running speed) was also derived. The equilibrium trim τ_e plus the inclination of the thrust line relative to the craft’s keel, e makes up the pitch angle, γ , appearing as input to the thrust and torque artificial neural networks. The thrust deduction factor ($1-t$) was incorporated in the surge equation above with a constant value of t equal to 0.03. We use the thrust deduction factor in order to include hull effects on the propeller operation or equivalently to include an increase of the hull’s viscous resistance due to the presence of the propeller in the aft part of the craft.

From the linear longitudinal motion block the linear speed of the planing craft can be derived by performing numerical integration of the surge equation:

$$\frac{dV_s}{dt} = \frac{T_{SPP} \cdot (1-t) \cdot p - D}{\Delta} \Leftrightarrow V_s = \int \left(\frac{T_{SPP} \cdot (1-t) \cdot p - D}{\Delta} \right) + V_{so} \tag{55}$$

where V_{SO} is the initial condition for linear speed of the planing craft.

The results obtained from the Savitsky general case method are shown in Figures 15 and 16.

Note that in this work the Savitsky general case script in MATLAB was used solely as a pre-processing computational utility. So, Figures 15 and 16 and the derived interpolated curves are incorporated in the overall model in MATLAB/Simulink as a lookup table with one input, which is speed V_s , and two outputs which are drag D and the equilibrium trim τ_e .

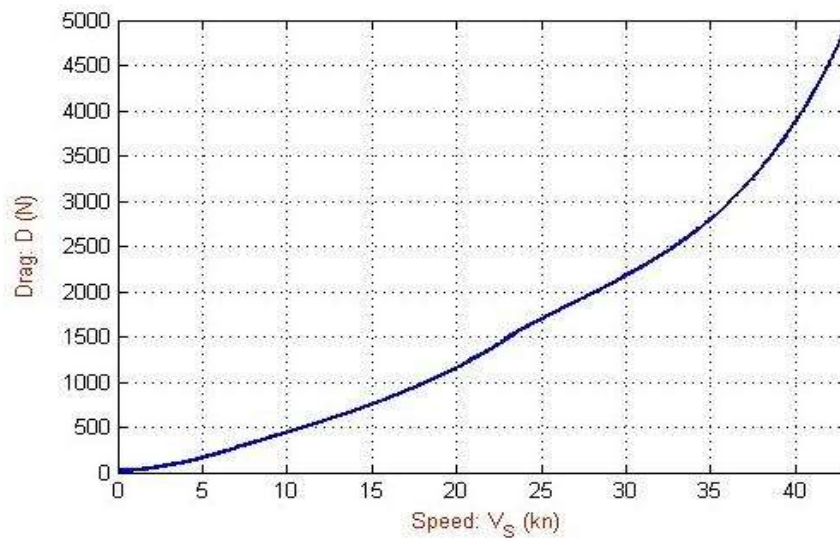


Figure 15. Resistance (drag) versus speed, according to the Savitsky general case method.

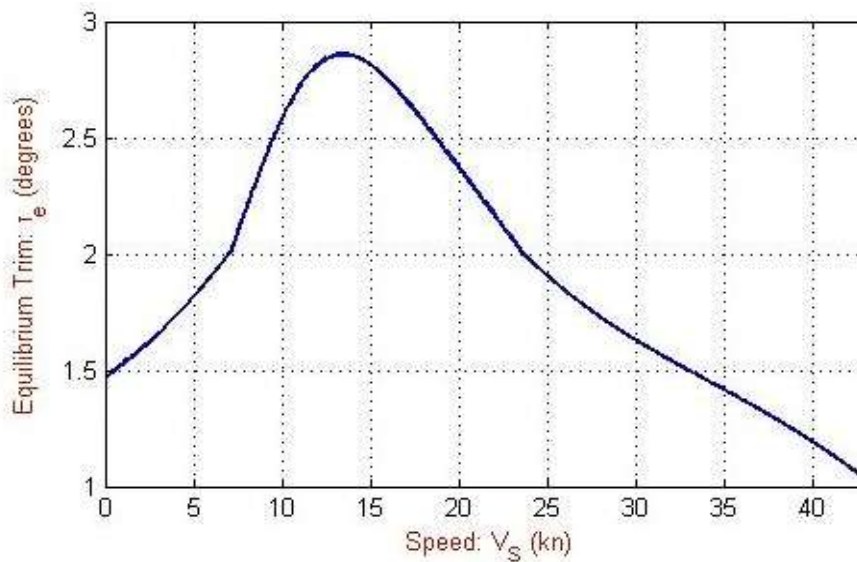


Figure 16. Equilibrium trim versus speed, according to the Savitsky general case method.

3. Results and Discussion

Numerical simulation runs were conducted to assess the ability of the developed model to respond to a step in the set-point (SP) as well as investigate the dynamic behavior of the propulsion plant during steady-state conditions. The set-point schedule and description of the simulations performed are summarized in Table 8.

The set-point schedule and rotor angular velocity versus time are presented in Figures 17 and 18 respectively. During the first 16 s, when acceleration of the AC motor was happening, the rotor angular velocity, ω_r , overshoots due to the slack of the PID controller to make fast corrections in the drive frequency. After the first 16 seconds, the rotor behavior in terms of angular velocity recovers to be more satisfactory both in transient and steady-state conditions.

Table 8. Simulation run schedule and description.

Time (Seconds)	SP (rpm) (Rotor Speed Command)	Explanation
0–16	0–3200	Start and acceleration of AC motor
16–100	3200	Warm up of AC motor
100	3200	Connection of SPP to AC motor *
100–165	3200	Start and acceleration of the hull
165–200	3200	Steady state condition at $V_S = 17$ kn (8.746 m/s)
200–270	3200–3500	Step (increase 300 rpm) of AC motor–Transient period of hull, propeller, AC motor
270–350	3500	Steady state condition at $V_S = 18$ kn (9.260 m/s)

* sudden connection of a stationary propeller to a rotate motor is theoretical and was applied for model evaluation purposes.

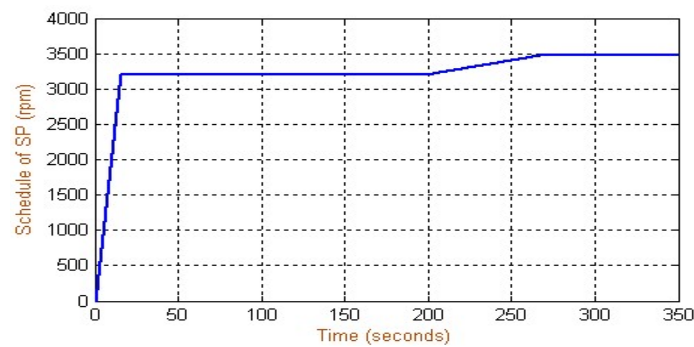


Figure 17. Set-point (SP) versus time.

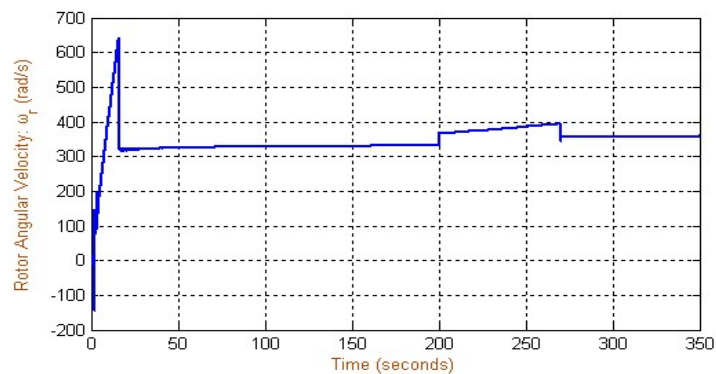


Figure 18. Rotor angular velocity versus time.

Drive frequency correction by the PID controller versus time is presented in Figure 19. As already discussed, during any step change of the set-point (0–16 s and 200–270 s) the controller is unable to follow adequately fast. This issue can easily be tackled by adding a pre-filter before the set-point signal is fed to the controller core. For all other operating conditions, the compensated system’s response is quite satisfactory and as shown in Figure 19. Indeed, note that frequency correction monotonically decreases, which means that the actual measured rpm of the rotor eventually converges to its set-point value.

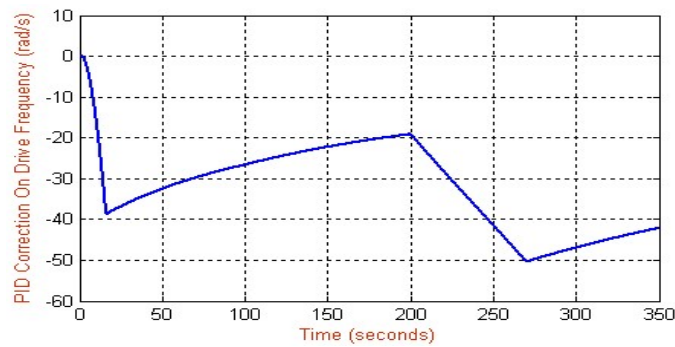


Figure 19. PID drive frequency correction versus time.

Mechanical load torque, T_m , and electromagnetic torque, T_e , versus time are shown in Figures 20 and 21 respectively. There is an initial settling phase of duration approximately 60 s required by the shaft vibrational model to converge. To accommodate for this, the SPP propeller is not coupled to the AC motor-shafting system until $t = 100$ s. During the first 100s-long interval the electromagnetic torque of the AC motor is close to zero with a pretty insignificant negative value. This small negative value during the initial settling transient means that the AC motor runs in regeneration/braking mode; it goes back into proper motor mode only after the SPP load is coupled. Indeed, after the coupling of the SPP with the system at $t = 100$ s, the load and electromagnetic torque come adequately close both in transient and steady-state phases.

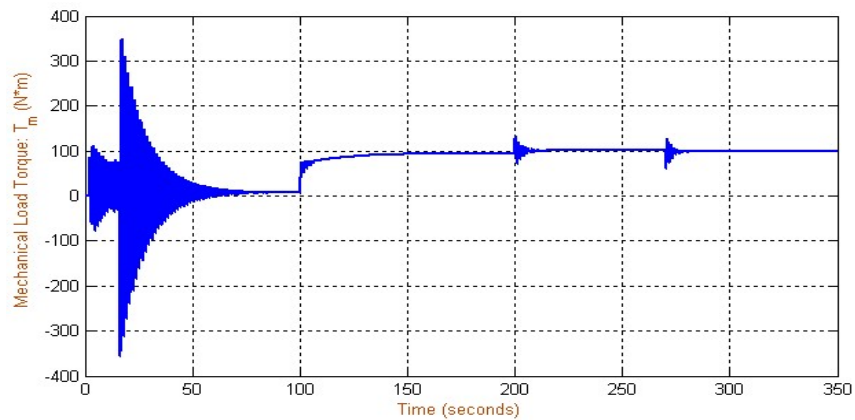


Figure 20. Mechanical load torque versus time.

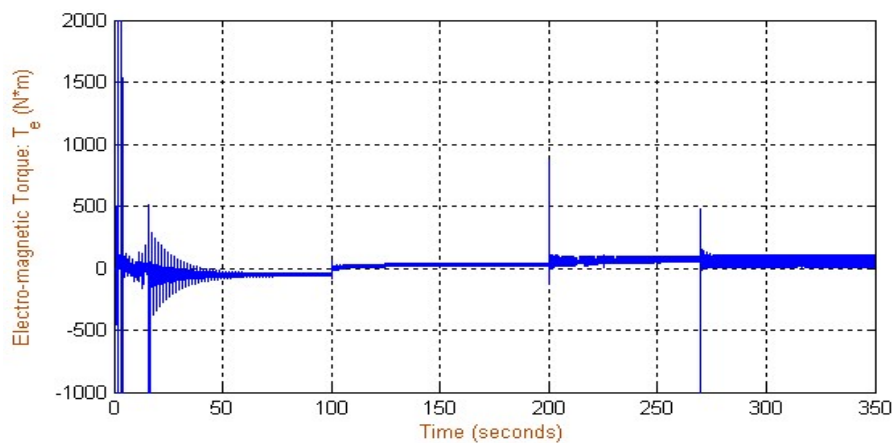


Figure 21. Electromagnetic torque versus time.

The drive frequency of the AC motor, f , versus time is given in Figure 22. As can be seen, the frequency follows faithfully the set-point schedule through the lookup table and after the necessary corrections applied by the PID controller.

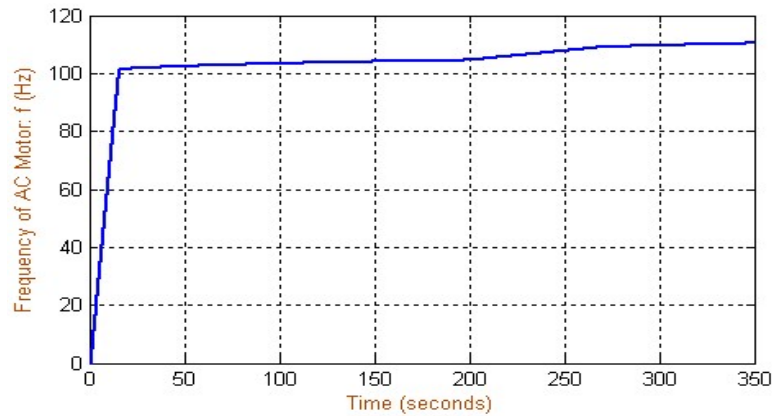


Figure 22. Drive frequency of AC motor versus time.

The watercraft’s speed, V_S , versus time is given in Figure 23. During the first 100 s of the simulation run, the velocity is zero because the SPP is not coupled with the AC motor and the hull is apparently stationary. After coupling occurs, the hull reaches a terminal speed of 17 knots and after the increasing set-point step of 300 rpm, the hull achieves a speed of 18 knots.

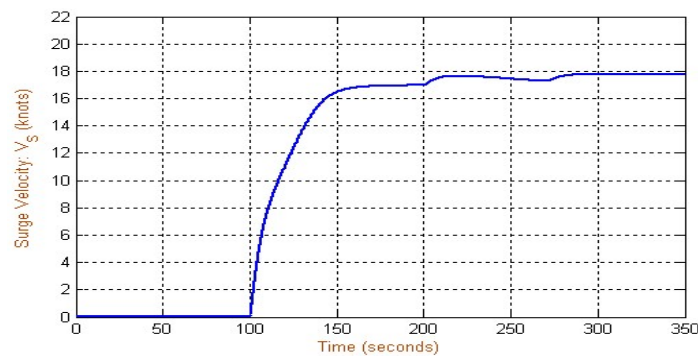


Figure 23. Speed versus time.

The drag D and equilibrium trim τ_e versus time are given in Figures 24 and 25 respectively. When the hull is stationary the drag is zero; it increases to gradually reach value 900 N when the hull achieves a speed of 17 knots. The drag increases further to almost 1000 N when the hull attains speed of 18 knots. On the other hand, equilibrium trim has a value of almost 1.5 degrees when the hull is not moving. This is due to a known limitation of Savitsky’s method, which cannot predict trim for speeds close to zero. However, after coupling the SPP with the rest of the system, equilibrium trim has a value of 2.7 degrees when the speed is 17 knots and 2.6 degrees when the speed is 18 knots.

SPP thrust and torque versus time are shown in Figures 26 and 27 respectively. They are zero from $t = 0$ s up to $t = 100$ s, since because the SPP is not coupled with the system yet. After this interval, the SPP thrust and torque demonstrate sufficiently smooth response in any transient or steady-state phase; furthermore, thrust steady state-value increases after the step set-point increase of 300 rpm is applied; in contrast, propeller torque steady-state value decreases. To explain this, one needs to account for the increase of propeller rotational speed, n , while the power influx delivered to the system remains constant. If, however, the active power influx to the motor were accordingly increased, then the SPP torque would remain the same or even correspondingly increase as a result.

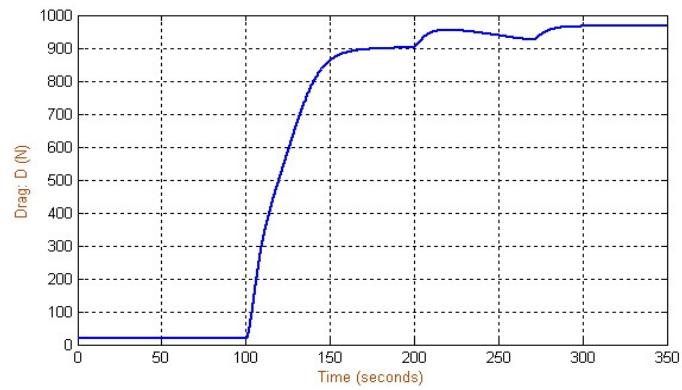


Figure 24. Drag versus time.

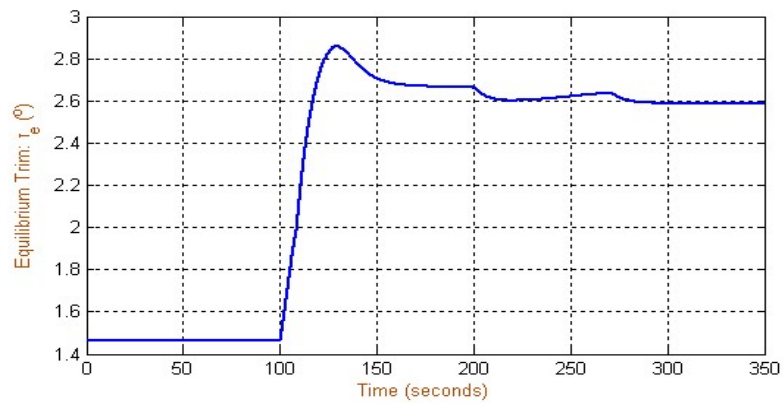


Figure 25. Equilibrium trim versus time.

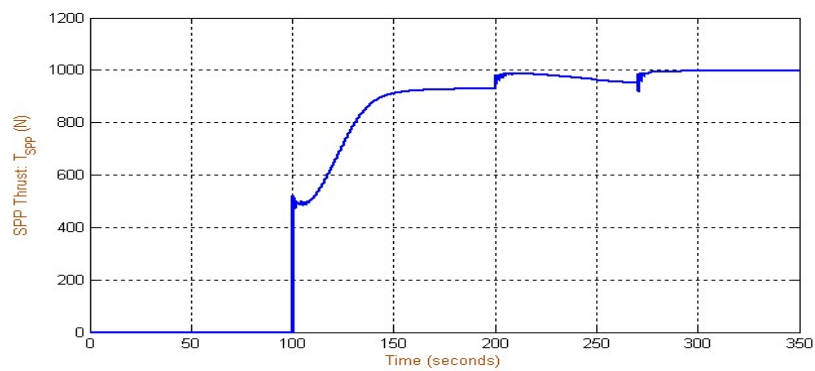


Figure 26. SPP thrust versus time.

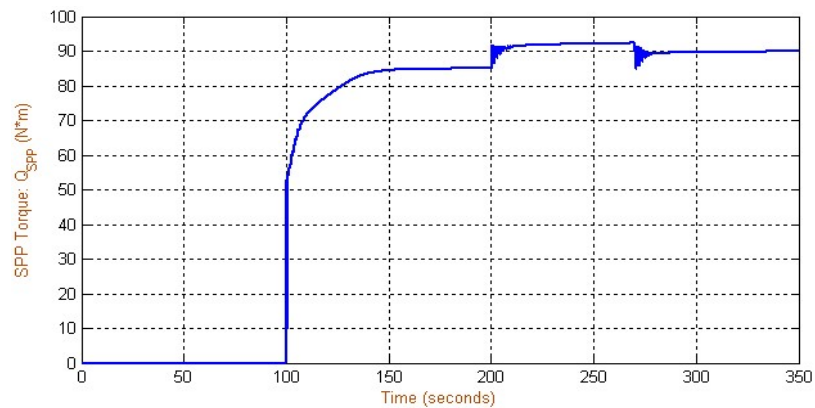


Figure 27. SPP torque versus time.

The rotational speed of SPP, n , versus time is shown in Figure 28. As mentioned above, for T_m and the shaft vibrational model there is a transient period of approximately 60 s; for this interval the rpm is arbitrary. Past this interval though, rpm reflects the transient and steady-state behavior per the other system variables.

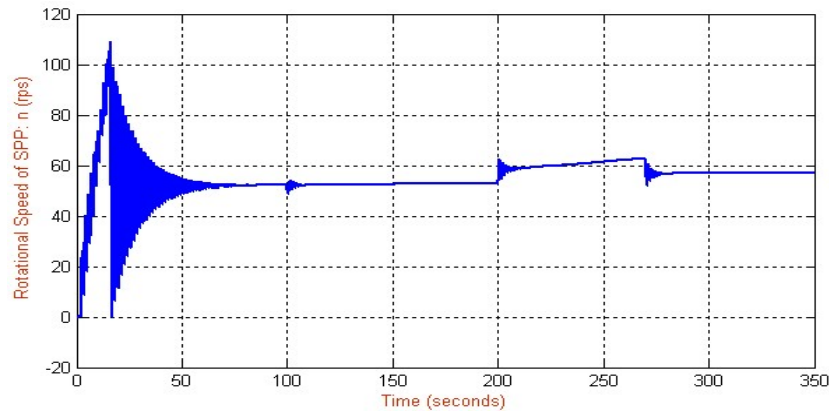


Figure 28. SPP rotational speed versus time.

Finally, the advance coefficient, J , versus time is given in Figure 29. It is zero from $t = 0$ s up to $t = 100$ s because the speed is zero and the hull is stationary. After $t = 100$ s the advance coefficient has a value of 0.68 when the hull achieves a speed of 17 knots and 0.65 when the speed is 18 knots. According to the test data for the SPP, the advance coefficient should be in the range 0.8 to 1.9.

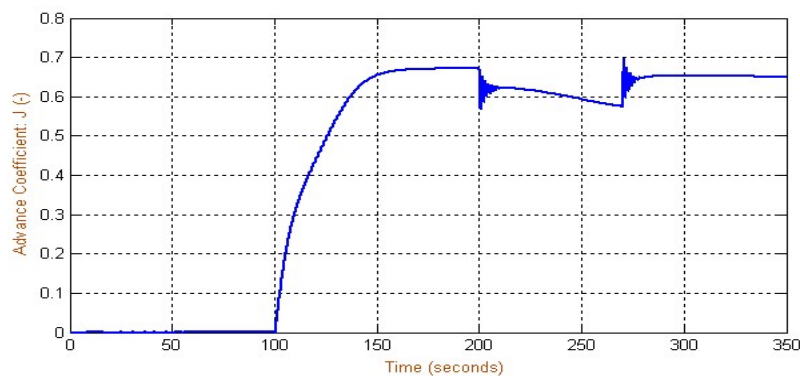


Figure 29. Advance coefficient versus time.

4. Conclusions

The following objectives were achieved by the research effort presented in this text:

- (a) A computer simulation model for a watercraft propulsion system was developed that enables modular swapping of arbitrary subsystem models.
- (b) A systematic methodology to derive continuous, at least in the service range of interest, performance curves for conventional or unconventional marine thrusters was developed; then, the methodology was extended to include ship resistance and propulsion data for planing-hull vessels.
- (c) An electric motor subsystem model, a finite-difference dynamic model for the propeller shaft, as well as neural networks employed as empirical models for a surface-piercing propeller and planing-hull watercraft were refined and joined together to form an overall computer simulation model with modular usability and flexibility.

Future work could involve refined controller tuning. Also, note that the advance coefficient range is overestimated by theoretical analysis as simulation results clearly demonstrate. This is the principal

reason why during neural net training for thrust and torque, we chose to employ separately propeller rotational speed, n , and speed of advance, U_A , instead of advance coefficient $J = U_A / (n D)$ that combines them. Specifically, the model predicts torque and thrust which effectively through dynamic simulation and model integration determine the corresponding rpm and forward speed. By keeping rpm and forward speed as separate variables, the model is not driven to assume any underlying implicit relationship but instead reveal them through simulations. This could also be considered in future work in order to achieve predictions for greater forward speed ranges with accurate estimates for the corresponding advance coefficient and rpm values.

Another avenue for future investigation is to refine the time steps required by the coupled sub-models involved in order to derive potentially reduced-order models especially for the electric motor and the shaft dynamics, i.e. the electromechanical subsystems. This can be achieved by introducing additional neural networks in combination with techniques inspired from singular value decomposition.

Author Contributions: Conceptualization, N.I.X. and V.T.; Formal analysis, N.I.X.; Investigation, N.I.X. and V.T.; Methodology, N.I.X. and V.T.; Supervision, N.I.X.; Validation, E.K.L.; Writing—original draft, N.I.X., V.T. and E.K.L.; Writing—review & editing, N.I.X. and E.K.L.

Funding: This research received no external funding.

Acknowledgments: The authors would like to express their gratitude to Justin M. Lorio and Karl D. von Ellenrieder for kindly providing the extensive SPP test data series from the experiments they performed while with the Dept. of Ocean and Mechanical Engineering of Florida Atlantic University. A special acknowledgment is also due to Burgi Engineers LLC, a company specializing in rotating machinery development, for kindly helping with various data about the electric motor.

Conflicts of Interest: The authors declare no conflict of interest.

Appendix A Configuration Specifics of Planing Hull

The main characteristics of the planing hull considered in this work are given in Table A1.

Table A1. Main characteristics of planing hull.

Specifications	US	CE
Length overall (LOA)	17'6"	5.28 m
Beam	6'11"	2.09 m
Deadrise	19°	19°
Approx. weight w/standard engine	1753 lbs.	795 kg
Estimated draft	2'11"	89 m
Fuel capacity	21 gal	79.5 l
Max passenger capacity	6	5
Max passenger weight	860 lbs.	390 kg

Also, Figure A1 shows a top and side view of the hull. As can be seen, the modified power system can be housed in either an inboard or outboard configuration depending upon the size of the motor, propeller and power transmission requirements. Appropriate modifications will be decided after the power supply system is selected as well. For our investigation, an inboard configuration was assumed.

In our case the power supply system was not specified. In future research and development efforts, however, the options to be considered include, but are not limited to, the following:

- (1) Generator set (outfitted with gasoline, diesel, natural gas or other type of engine as prime mover);
- (2) Battery bank;
- (3) Fuel cell system incl. hydrogen and oxygen storage;
- (4) Hybrid configuration(s).

To take full advantage of the existing general arrangement, one will need to consider the locations of the existing fuel tanks as well as their capacity and what parts of the alternative powerplant can be

accommodated in an outboard configuration. As already mentioned, this hull design effort will be part of future research.



Figure A1. Top and side view of planing hull.

References

1. *Marine Engineering*; Harrington, R.L. (Ed.) Society of Naval Architects and Marine Engineers Press: Atlantic City, NJ, USA, 1992.
2. Lorio, J.M. Open water testing of a surface piercing propeller with varying submergence, yaw angle and inclination angle. Master's Thesis, Department of Ocean Engineering, Florida Atlantic University, Boca Raton, FL, USA, May 2010.
3. Zisman, Z.S. On the Simulation of an All Electric Ship Powertrain Utilizing a Surface Piercing Propeller Via a Modular Main Propulsion Plant Model. Master's Thesis, Department of Aerospace & Ocean Engineering, Virginia Tech, Blacksburg, VA, USA, May 2011.
4. Von Ellenrieder, K. Open Water Towing Tank Testing of a Surface Piercing Propeller. Presented at the 29th American Towing Tank Conference, Annapolis, MD, USA, August 2010.
5. Sul, S.-K. *Control of Electric Machine Drive Systems*; IEEE Press: Piscataway, NJ, USA, 2011.
6. Xiros, N.I. *Robust Control of Diesel Ship Propulsion*; Springer: London, UK, 2002.
7. Savitsky, D. Hydrodynamic design of planing hulls. *Mar. Technol.* **1964**, *1*, 71–95.
8. Nazarov, A. On application of parametric method for design of planing craft. Presented at the 3rd Chesapeake Power Boat Symposium, Moscow, Russia, January 2012.

